Hindawi
International Journal of Energy Research
Volume 2024, Article ID 1155917, 16 pages
https://doi.org/10.1155/2024/1155917

Research Article

Engineering of Multidimensional Core-Shell Perovskite Precursors to Obtain Superior Luminescence and Incorporating in Luminescent Solar Concentrators

Elnaz Bagherzadeh-Khajehmarjan,[1] **Sohrab Ahmadi-Kandjani**,[1,2,3] **Nasim AmirKooshesh**,[2] **and Sajjad Rajabi-Ghaleh**[2]

[1]*Research Institute for Applied Physics and Astronomy, University of Tabriz, 51666-14766 Tabriz, Iran*
[2]*Department of Physics, University of Tabriz, Tabriz, Iran 51666-14766*
[3]*Photonics center of excellence, University of Tabriz, Tabriz, Iran 51666-14766*

Correspondence should be addressed to Sohrab Ahmadi-Kandjani; s_ahmadi@tabrizu.ac.ir

Received 29 August 2023; Revised 2 January 2024; Accepted 10 January 2024; Published 23 January 2024

Academic Editor: Sejoon Lee

The luminescence feature of perovskite NPs with high PLQY directs them to lighting and display applications. 2D $(A)_2MA_{n-1}Pb_nBr_{3n+1}$ $(n = 1 - 6)$ perovskites with A as octylammonium and benzylammonium cations are synthesized by the LARP method, in which the highest PL emission is attained to the $n = 6$ sample with benzylamine cation. XRD results reveal the appearance of diffraction peaks related to 3D perovskites with increasing n value. Mixing 3D perovskites with 2D ones leads to the formation of core-shell $MAPbBr_3 - (A)_2MA_{n-1}Pb_nBr_{3n+1}$ $(n = 1 - 6)$ nanostructures, confirmed by TEM images and optical properties. Incorporation of Zn to core-shell perovskites improves the PL intensity and induces higher crystallinity. A blue shift in absorption and emission spectra of Zn-doped perovskites is observed. The highest PLQY (94%) is attributed to the Zn-doped core-shell perovskite with $n = 6$ among the all-synthesized samples. Luminescent solar concentrators with thicknesses of 2 mm and 5 mm are fabricated with benzylamine-based perovskites, because of their greater PLQY versus octylamine-based perovskites. The performance of LSC devices is boosted for the LSC with 5 mm thickness. The relative PCE obtained for the core-shell perovskite-based LSC with thickness of 5 mm reaches to almost 60%.

1. Introduction

Perovskite quantum dots (QDs) have received much more attention in optoelectronic applications [1–4] due to their higher photoluminescence quantum yield (PLQY) relative to thin films, narrow full width at half maximum (FWHM), ease of solution processability, and low-cost synthesis procedure [5, 6]. 3D perovskite QDs with an ABX_3 structure possess astonishing electrical and optical properties while suffering from low stability [7, 8]. To overcome this challenge, mixing 3D perovskites with 2D ones could be promising. 2D perovskites are among the low-dimensional perovskites with outstanding optoelectronic properties originating from quantum confinement effects and their exciton binding energies [9]. 2D perovskites with a formula $(A)_2(MA)_{n-1}M_nX_{3n+1}$ $(1 \leq n < \infty)$ demonstrate higher water resistance and a longer lifetime, where A is a long organic cation [10, 11]. For $n = 1$, the structure is pure 2D perovskite, while mixed-dimensional (2D/3D) perovskite will appear by increasing n. $n = \infty$ belongs to the pure 3D perovskite [12]. Conducting the synthesis of QDs at room temperature and the simplicity and low cost of the synthesis process are the factors that make the ligand-assisted reprecipitation (LARP) strategy more efficient than the hot-injection procedure [13]. Incorporation of octylamine (OA) and oleic acid as ligands in the LARP method during the synthesis of $MAPbBr_3$ QDs enhances the PLQY up to 70% [14]. Altering the molar ratio of perovskite precursors without changing the ligands also influences the size and PLQY of QDs, as the highest PLQY (about 80%) is achieved for the QDs with

a size of 3.3 nm [15]. The carbon length of the organic amines and also the reaction temperature of the synthesis procedure are the factors affecting the morphology, stability, and PLQY of perovskite nanocrystals (NCs) [16, 17]. To improve stability, the synthesis of 2D perovskite colloidal nanoparticles (NPs) with high PLQY has appealed widespread focus [18–20]. 2D perovskite ($n = 1 - 6$) QDs with 1-butylammonium as a long organic cation and an average size of 10 nm are synthesized for Br and I halides. The enhanced optical stability with respect to 3D counterparts and also a relative high PLQY (48.6%) for the 2D perovskites with $n = 6$ and Br halide are the features of the synthesized QDs [21].

Growing a shell with a higher bandgap around a semiconductor nanostructure is one of the strategies to improve photoluminescence and stability [22, 23]. There are some kinds of core-shell structures, such as semiconductor-organic passivator core-shell, semiconductor-semiconductor hetero structure, perovskite-inorganic protective layer core-shell, and chalcogenide quantum dot-perovskite core-shell [24]. Capping ZnO NPs with polyvinylpyrrolidone polymer enhances the spectral purity and reduces the quantum efficiency [25]. However, a balanced photocatalytic and quantum efficiency are obtained in silica-encapsulated ZnO QDs [26]. Defect states, Forster resonance energy transfer (FRET), and charge transfer (CT) are the dominant phenomena in the PL quenching of surface-modified ZnO nanoplates [27]. Perovskite-perovskite core-shell NPs belong to the semiconductor-semiconductor core-shell type [24]. Bhaumik et al. [28] succeeded in synthesizing perovskite-perovskite core-shell NPs with 3D $MAPbBr_3$ as a core and 2D $(OA)_2PbBr_4$ perovskite as a shell. Besides possessing a high PLQY (92%), the synthesized core-shell structures are stable even after two months. Study of the nonlinear optical properties of the synthesized multidimensional core-shell perovskite exhibits a giant five-photon absorption [29]. Incorporation of MA-OA core-shell perovskites in polymethyl methacrylate (PMMA) polymer matrix results in PL stability after fully immersing in water for 18 h [30]. Inorganic Cs-based core-shell $CsPbBr_3$/Cs_4PbBr_6 structures demonstrate a 12% enhancement in PLQY with respect to the control $CsPbBr_3$ seeds. Furthermore, the PL intensity of the synthesized core-shell perovskites drops to half of its maximum intensity after 7 days, while PL quenching occurs in 2 days for the bare $CsPbBr_3$ [31]. The water resistance of $CsPbBr_3$/$CsPb_2Br_5$ core-shell perovskite is proved by the addition of water into the perovskite solution, in which the NCs still emit a green color after being sonicated for 2 h [32].

Substituting metal halides such as Cu, Sn, Mn, and Zn with outstanding properties of nontoxicity, stability, and earth abundance for Pb-based halides could obtain achievements in the optoelectronic properties of metal halide perovskites [33]. Organic copper halides with high PLQY up to 92% are good candidates for X-ray scintillators [34]. PLQYs up to 25% and 23% are reported for organic-inorganic Cu- and Zn-based metal halides with potential applications in fingerprint detection [35, 36]. A study on different morphologies of ZnO nanostructures reveals that visible emission from these nanostructures originates from oxygen-related adsorbed species [37]. The ZnO nanostructure dimension is also varied by the hydroxide ion concentration of precursors, which affects the surface defect states and hence the QY [38]. Factors such as surfactants, dopants, precipitating agents, and fluxing agents during the synthesis process of rare earth-doped phosphors affect the product's crystallinity and morphology and hence the luminescence [39]. In perovskite structures, doping Zn is also a promising approach to achieve uniform morphology, improved stability, and higher PL intensity [40, 41]. Due to the hazardous risks of lead to humans and the environment, a beneficial step is reducing the amount of Pb in perovskite-based optoelectronic devices. The presence of Zn in the 2D $(OA)_2SnX_4$ (X = Br, I) perovskite lattice leads to highly qualified morphology and boosted stability. The PLQY of the synthesized 2D perovskites is increased to 85% and 50% for Br- and I-based perovskites, compared to the bare ones [42]. The photovoltaic performance of fabricated solar cells based on Zn-doped $MAPbI_3$ is improved to 18.18%, while the efficiency of a control solar cell is 17.44%. Reduced J-V hysteresis is another advantage of Zn-doped perovskite-based solar cells [43]. Strategies to enhance the PL emission of perovskite-based materials are utilized in lighting, lasing, and display applications [44–46]. Highly luminescent perovskites are also a good candidate to be developed in luminescent solar concentrators (LSCs). A polymeric matrix with fluorophores doped in it is called LSC, in which the incident light can be absorbed and emitted by the fluorophores. The emitted light could be guided to the LSC edges by total internal reflection, where the solar cells are attached [47]. The micron-sized $MAPbBr_3$ perovskites, synthesized by a sonochemical procedure, are utilized in bulk LSCs by our group [48]. The LSC geometry also influences the PCE in LSC devices, where half-cylindrical LSCs based on $MAPbBr_3$ QDs demonstrate higher PCEs with respect to sheet LSCs [49]. The strong, stable LSCs based on highly luminescent (99.4%) $CsPbI_3$ perovskites demonstrate an optical efficiency of 3.1% [50]. The integration of a 0D perovskite-based LSC into a motor fan gives the opportunity to drive a real device with LSCs for the first time [51]. The modified synthesis of iodine-based 2D perovskites improves the PLQY to 56%, and its incorporation into LSC enhances the optical efficiency up to 2.0% [52].

In this work, 2D perovskite NPs with octylammonium (OA) and benzylammonium (BZA) long organic cations are synthesized with different values of n ($n = 1 - 6$). The highest PLQY in this category belongs to the perovskite, with $n = 6$. Mixing 2D perovskites with 3D ones leads to the formation of a core-shell structure with enhanced PLQY compared to the first category. The third category is formed by doping $ZnBr_2$ into mixed 3D-2D perovskites, in which further enhancement of the luminescence emission is achieved. Incorporation of prepared samples with $n = 6$, as luminescent materials, into LSCs leads to enhanced PCE of the LSC devices.

2. Experimental Section

2.1. Materials. Methylamine (MA, 40 wt% in water), octylamine (OA, ≥98%), benzylamine (BZA, >99%), hydrobromic acid (HBr, 48 wt% in water), lead bromide ($PbBr_2$, ≥98%), oleic acid (89–95%), oleylamine (70%), toluene (≥99.9%),

and N, N-dimethyl formamide (DMF, ≥99.9%) from Merck are utilized to synthesize 2D and 3D perovskite NPs. Methyl methacrylate (MMA, 99%), polymethyl methacrylate (PMMA, Mw = 996000), and photo initiator diphenyl (2,4,6-trimethylbenzoyl) phosphine oxide (TPO, 97%) are utilized in the fabrication process of LSC polymeric matrix.

2.2. Synthesis Procedure

2.2.1. 2D Layered Perovskites. Before the perovskite synthesis, it is a priority to synthesize alkyl ammonium salts. MABr, OABr, and BZABr salts are prepared by reacting alkyl amine and HBr in an equal molar ratio, as mentioned in Ref [15]. The LARP procedure for the synthesis of 2D bromide perovskites follows Ref [21], where the butyl amine is used as a long ammonium cation. The long organic ammonium cations in this work are OA and BZA. In brief, to synthesize 2D perovskites with $n = 1$, the precursor is prepared by reacting 0.2 mmol $PbBr_2$, 0.4 mmol OABr, 50 μL oleylamine, and 0.5 mL oleic acid in 5 mL DMF. Injection of 50 μL precursor solution in 5 mL of toluene under vigorous stirring results in 2D perovskite synthesis. The $(OA)_2PbBr_4$ NPs are obtained after centrifugation for 10 min. To synthesize 2D perovskites with higher values of n, the precursor solution is prepared by mixing different molar ratios of MABr, OABr, and $PbBr_2$, with the molar ratio of $PbBr_2$ at 0.04 mM. The quasi-2D perovskite NPs are obtained by injecting the precursor solution into toluene. The same process is repeated for the 2D perovskites with BZA cations.

2.2.2. Core-Shell 3D-2D Perovskites. The synthesis of multidimensional 3D-2D perovskites is conducted according to Ref [29]. First, the 3D perovskite precursor is prepared by adding 0.16 mmol MABr, 0.2 mmol $PbBr_2$, 50 μL oleylamine, and 0.5 mL oleic acid to 5 mL DMF. The 2D precursor solutions ($n = 1 - 6$) are also obtainable, as pointed out in Section 2.2.1. Second, the 3D precursor solution is injected into 5 mL toluene under stirring, alongside the 2D $(OA)_2PbBr_4$ precursor. 3D and 2D precursors are added to toluene, just as though the molar ratio of MA in the 3D precursor to OA in the 2D precursor is 8 : 2. The 3D-2D core-shell $MAPbBr_3$-$(OA)_2PbBr_4$ NPs are then attainable after centrifugation. For the synthesis of other (3D-2D) $MAPbBr_3 - OA_2MA_{n-1}Pb_nBr_{3n+1}$ nanoperovskites with n, the 2D precursor solutions are prepared with molar ratios related to each n. The amounts of 3D and 2D precursors poured into toluene have the same molar ratio of 8 : 2. The synthesis procedure of BZA-based 3D-2D perovskites is the same as that of OA ones.

2.2.3. Zn-Doped 3D-2D Perovskites. It is demonstrated that the presence of Zn influences the luminescence of 3D perovskites, positively [43]. To enhance the PLQY of multidimensional 3D-2D perovskites, the synthesis procedure of the 3D precursor solution is modified. A Zn-doped 3D precursor is prepared by the addition of $PbBr_2$ and $ZnBr_2$ in a molar ratio of 9 : 1. The modified 3D precursor is prepared by mixing organic and inorganic parts in equivalent amounts (0.2 mmol MABr, 0.18 mmol $PbBr_2$, and 0.02 mmol $ZnBr_2$). The amount of other materials is constant. Therefore, the Zn-doped 3D-2D perovskites are synthesized according to Section 2.2.2, in which the 3D precursor is modified to a Zn-doped 3D precursor.

2.3. LSC Fabrication. The fabrication of LSC devices is accompanied by photopolymerization process. PMMA is dissolved in MMA with a weight ratio of 3 : 7 (PMMA/MMA) at 60°C. Then, the photo initiator, TPO, with a weight ratio of 1% with respect to the total mixture is added [53]. The perovskites with BZA cations are used as luminescent fluorophores in LSCs due to their higher PLQY compared with OA-based perovskites. The perovskite samples are dried under vacuum before their incorporation into polymeric solutions. Afterward, the solution is poured into a mold consisting of two glass sheets with polyvinyl chloride (PVC) gasket as a spacer. The gasket determines the mold thickness, which is 2 mm and 5 mm in our LSCs. To complete the photopolymerization, the mold is illuminated by a UV lamp for 2-5 hours, depending on the mold thickness. Finally, the polymeric samples are cut into $50 \times 40 \times 5\,mm^3$ and $50 \times 40 \times 2\,mm^3$ using a laser cutter. In order to deduce the perovskite influence on LSC performance, the pure PMMA LSCs with thicknesses of 2 mm and 5 mm are also fabricated.

2.4. Characterization. Shimadzu UV-2450 spectrophotometer and Jasco FP-6200 spectrofluorometer are the instruments used for measuring the optical properties of synthesized perovskites. All the samples are diluted in the same concentration in toluene, and their absorption and PL spectra are measured in the quartz cell. For the PLQY measurements, the absorption and PL spectra for each sample are measured at different concentrations in the quartz cell. The same measurements are done for the reference dye, and then, the PLQYs are calculated, as will be mentioned in detail in Section 3.4. X-ray diffraction (XRD) patterns help to investigate the structural properties of the samples, attained by Siemens D500 and Tongda TD-3700 for OA- and BZA-based perovskites, respectively. To determine the size of synthesized perovskite NPs, Philips EM 208S transmission electron microscopy (TEM) is employed.

For electrical characterization, the LSC is illuminated by a metal halide lamp (HQI-BT 400 W/D PRO, Osram). Figure 1 shows the lamp spectrum. According to the standards of LSC measurements, the LSC is placed on a black background to minimize the light reflections [54]. A solar panel (AK5318) with a dimension of $3.8 \times 0.5\,cm^2$ and characteristics of 0.5 V and 160 mA is attached to the LSC. The characterization of LSC devices is measured by a Keithley 2410 source meter, which is connected to a computer.

3. Results and Discussion

3.1. Structural Properties. XRD patterns of the synthesized perovskites drop-cast on the substrate are employed to study the crystal structure of the samples. Figure 2 demonstrates the XRD patterns of 2D perovskites ($A_2MA_{n-1}Pb_nBr_{3n+1}$), where A is OA or BZA, and their mixture with 3D $MAPbBr_3$

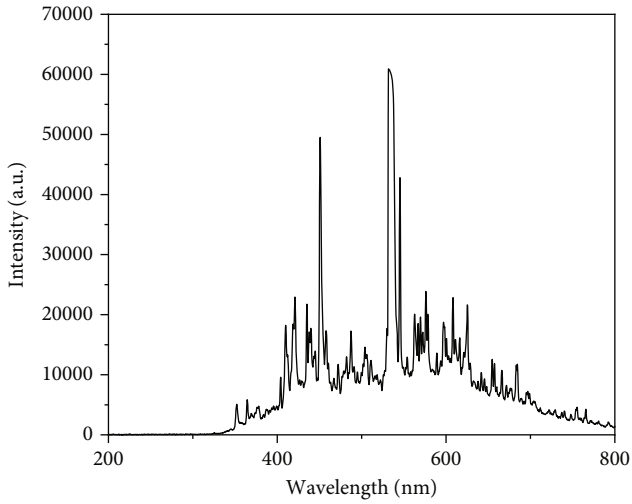

Figure 1: Metal halide lamp spectrum for characterization of LSC devices.

ones. As shown in Figures 2(a) and 2(b), the peaks at angles below 14° belong to 2D perovskites, relating to (00n) planes (where $n = 2, 4, 6, \cdots$) [55–57]. The position of these peaks and their d-spacing are presented in Table 1. The calculated d-spacing for the (002) peak located at 6.14° is obtained 14.38 Å for $(OA)_2PbBr_4$, while it increases for OA-based 2D perovskites with $n \geq 3$. It is also observable that multiple diffraction peaks (at angles below 14°) for the 2D OA-based perovskites with higher n values originate from the presence of lower n value perovskites in the composition, as shown in Figure 2(b) [56, 58]. Furthermore, the quasi-2D OA-based perovskites with $n \geq 3$ exhibit a weak diffraction peak at 14.9°, relating to the (100) peaks of 3D $MAPbBr_3$ perovskite [59]. It is noteworthy to mention that regardless of the composition of the perovskite precursor, the quasi-2D perovskite films consist of large n-phases ($n \longrightarrow \infty$) or 3D perovskites [60]. For the multidimensional 3D-2D perovskites, the peaks at lower angles ($2\theta < 14.9°$) still exist for $n = 1$ and $n = 2$ samples, as shown in Figures 2(c) and 2(d). Furthermore, weak XRD peaks positioned at 14.9° and 30° are observable for multidimensional perovskites with $n = 1$ and 2 that are intensified with increasing n values. These peaks are related to 3D perovskite formation [28]. It means that by increasing the n value and hence decreasing the fraction of OA cation, the crystal structures of the 3D-2D samples resemble 3D perovskites [61]. In addition to lower angle peaks (belonging to 2D perovskites), Zn-doped 3D-2D perovskites possess diffraction peaks of 3D $MAPbBr_3$ perovskites, located at 14.9° and 30°. The intensity of the peaks below 14° is diminished for the Zn-doped 3D-2D OA-based perovskites with increasing n values. The presence of the peak at 13.8° for the Zn-doped 3D-2D OA-based perovskite with $n = 4$ in Figure 2(d) represents the existence of 2D perovskite with $n = 4$ in this sample. It reveals that some 2D perovskites are present separately during the synthesis process of mixed 3D-2D perovskite. To investigate the effect of Zn doping on the crystal structure of perovskites, XRD patterns of the bare and Zn-doped $MAPbBr_3$ are given in Figure 2(e). It is clearly apparent that the incorporation of Zn with small ion radii intensifies the XRD peaks of the 3D perovskite significantly. Narrower diffraction peaks in Zn-doped sample promise higher crystallinity [62]. Figure 2(f) demonstrates the diffraction peaks of 2D $(BZA)_2PbBr_4$ perovskite matching the (00n) planes of pure 2D perovskites [20, 63]. Calculation of interlayer spacing for the (002) plane of $(BZA)_2PbBr_4$ at an angle 5.02° results in 17.60 Å, which is in consistence with literature [64]. The d-spacing for quasi-2D BZA-based perovskites ($n = 1 - 6$) is given in Table 2. The XRD peaks for quasi-2D BZA perovskites with $n \geq 3$ are given in Figure 2(g). It is found out that the peaks of 2D BZA-based perovskites with $n = 2$ located at angles below 14° are present in the XRD peaks of $n = 4$ sample. In addition, the 2D BZA-based perovskites with $n = 5$ and $n = 6$ also contain the peaks of the perovskite with $n = 3$. It confirms the presence of lower n value phases in quasi-2D BZA-based perovskites with $n \geq 4$ [58]. Despite the existence of lower angle peaks ($2\theta < 14°$) associated with the layered structure of 2D perovskites, the appearance of 3D perovskite peaks is observed in Figures 2(h) and 2(i) for bare and Zn-doped 3D-2D BZA-based perovskites. The lower angle peaks related to 2D layered structures are weak for the multidimensional BZA-based perovskites with $n = 6$, representing their crystal structure resembling to 3D ones.

3.2. Size Distribution. TEM images help to prove the formation of core-shell structure in mixed 3D-2D perovskites. For instance, the TEM images of 3D-2D $MAPbBr_3 - (OA)_2MA_{n-1}Pb_nBr_{3n+1}$ ($n = 6$) and Zn-doped $MAPbBr_3 - (BZA)_2MA_{n-1}Pb_nBr_{3n+1}$ ($n = 6$) NPs are demonstrated in Figures 3(a) and 3(b), suggesting a core-shell structure for several NPs. The core-shell NPs are circled, and the cores are recognized via the darker region. Accordingly, the formation of core-shell nanostructures is affirmed by the contrast in TEM images. The electron density contrast between the core $MAPbBr_3$ and the shell 2D perovskite with $n = 6$ is low because of the similarity of quasi-2D perovskites with higher n values to 3D ones [28]. Consequently, a vivid TEM image for 3D-2D $MAPbBr_3$-$(BZA)_2PbBr_4$ ($n = 1$) is obtained (Figure 3(c)). The nanoparticle size distribution is also depicted in Figure 3(d), representing the overall particle size of 5.6 nm. The core-shell structures are indicated by red circles in Figures 3(a)–3(c).

3.3. Optical Properties. The absorption spectra of the synthesized perovskites based on OA and BZA are illustrated in Figure 4. For 2D $(OA)_2MA_{n-1}Pb_nBr_{3n+1}$ perovskite with $n = 1$, a strong exciton peak placed at 398 nm is observed [65]. For $n = 2$, the peak red shifts to 430 nm, and a shoulder at 370 nm exists (Figure 4(a)). The shoulder at $n = 2$ turns into a peak for perovskites with $n \geq 3$, suggesting the presence of a small fraction of perovskites with lower n values. The difference in absorption spectra of 2D OA-based perovskites with higher n values is not obvious, as reported in Figure 4(a) [66]. However, the red shift in absorption peaks of 2D BZA perovskites is more noticeable with increasing n values (Figure 4(d)).

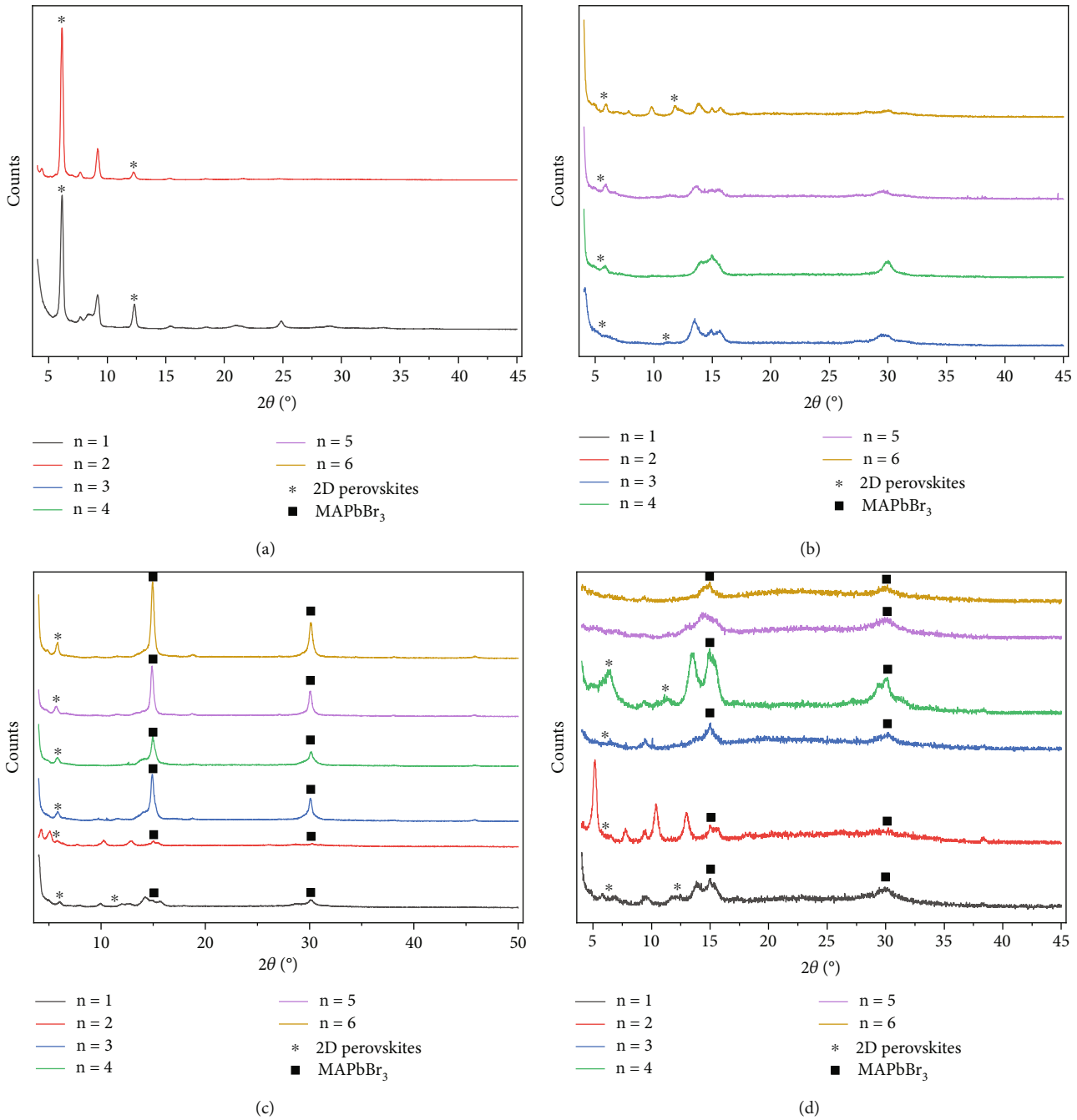

Figure 2: Continued.

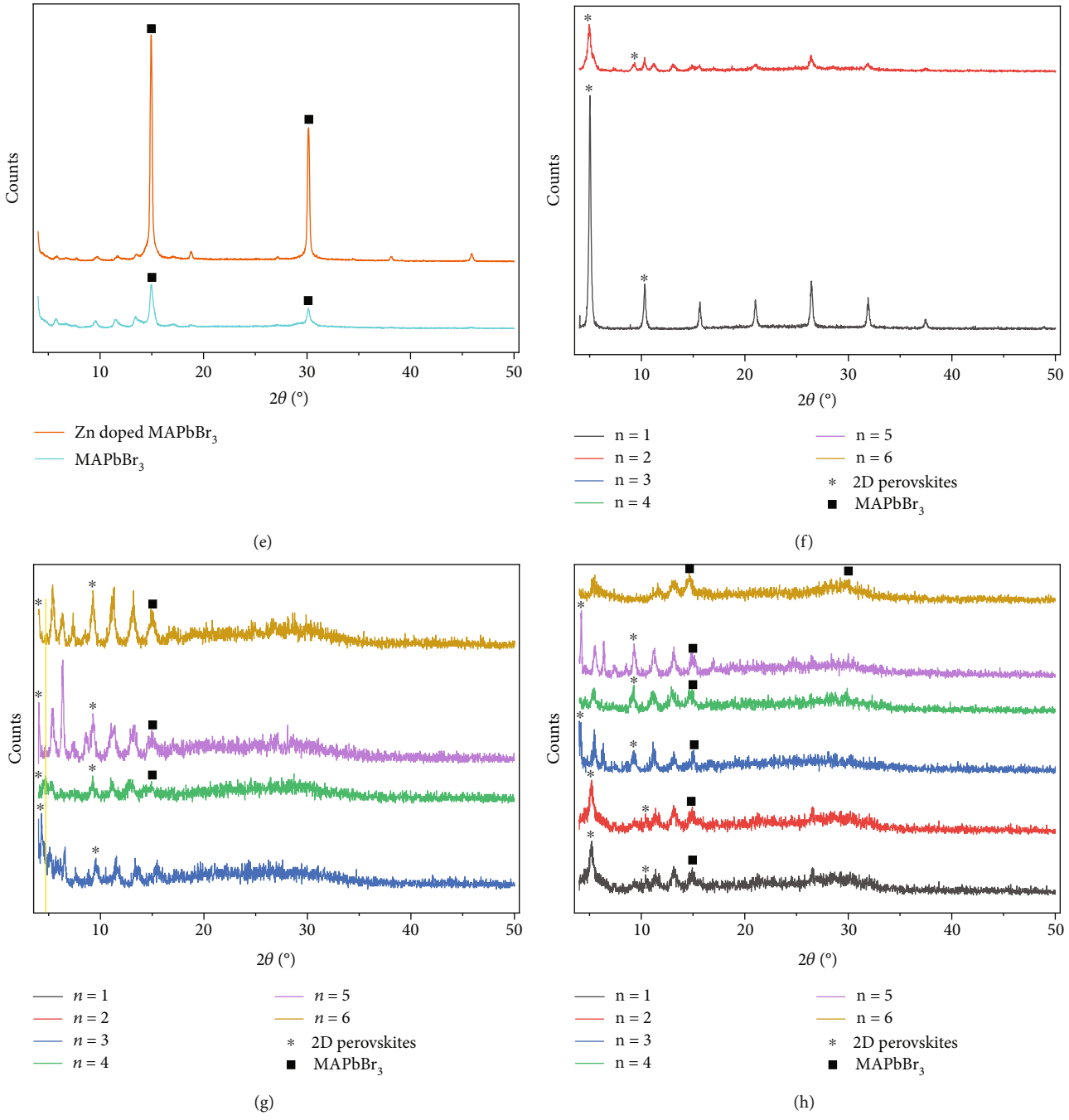

Figure 2: Continued.

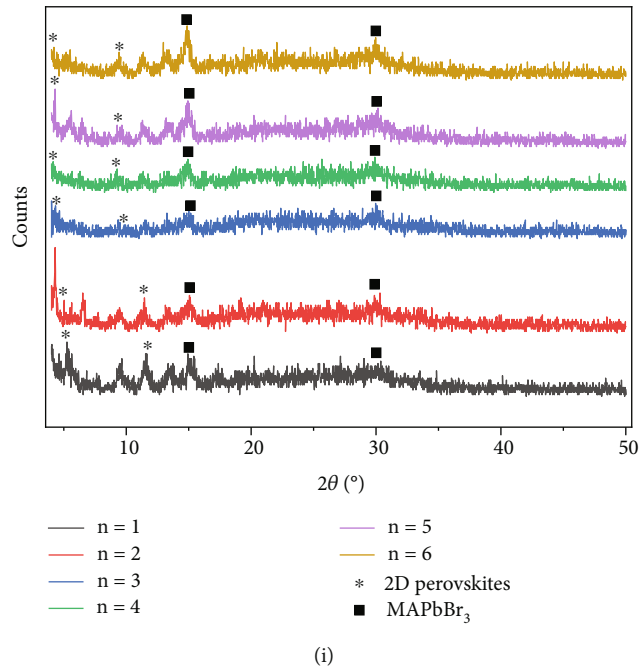

(i)

FIGURE 2: XRD patterns of (a) 2D $(OA)_2MA_{n-1}Pb_nBr_{3n+1}$ with $n = 1, 2$, (b) 2D $(OA)_2MA_{n-1}Pb_nBr_{3n+1}$ with $n = 3 - 6$, (c) 3D-2D $MAPbBr_3 - (OA)_2MA_{n-1}Pb_nBr_{3n+1}$ $(n = 1 - 6)$, (d) Zn-doped $MAPbBr_3 - (OA)_2MA_{n-1}Pb_nBr_{3n+1}$ $(n = 1 - 6)$, (e) $MAPbBr_3$ and Zn-doped $MAPbBr_3$, (f) 2D $(BZA)_2MA_{n-1}Pb_nBr_{3n+1}$ with $n = 1, 2$, (g) 2D $(BZA)_2MA_{n-1}Pb_nBr_{3n+1}$ with $n = 3 - 6$, (h) 3D-2D $MAPbBr_3 - (BZA)_2MA_{n-1}Pb_nBr_{3n+1}$ $(n = 1 - 6)$, and (i) Zn-doped $MAPbBr_3 - (BZA)_2MA_{n-1}Pb_nBr_{3n+1}$ $(n = 1 - 6)$ perovskites. The peaks related to $(00n)$ planes of 2D perovskites and also (100) and (200) planes of 3D $MAPbBr_3$ are marked with star and square in the XRD patterns, respectively.

TABLE 1: Miller indices and d-spacing for $(OA)_2MA_{n-1}Pb_nBr_{3n+1}$ with $n = 1 - 6$.

	$(OA)_2MA_{n-1}Pb_nBr_{3n+1}$ $(n = 1)$		$(OA)_2MA_{n-1}Pb_nBr_{3n+1}$ $(n = 2)$		$(OA)_2MA_{n-1}Pb_nBr_{3n+1}$ $(n = 3)$		$(OA)_2MA_{n-1}Pb_nBr_{3n+1}$ $(n = 4)$		$(OA)_2MA_{n-1}Pb_nBr_{3n+1}$ $(n = 5)$		$(OA)_2MA_{n-1}Pb_nBr_{3n+1}$ $(n = 6)$	
Reflection	2θ (°)	d (Å)	2θ (°)	d (Å)	2θ (°)	d (Å)	2θ (°)	d (Å)	2θ (°)	d (Å)	2θ (°)	d (Å)
(002)	6.14483	14.38	6.12733	14.42	5.807	15.21	5.8235	15.17	5.8235	15.17	5.87383	15.04
(004)	12.32667	7.18	12.20767	7.25	11.24567	7.86					11.88633	7.44

TABLE 2: Miller indices and d-spacing for $(BZA)_2MA_{n-1}Pb_nBr_{3n+1}$ with $n = 1 - 6$.

	$(BZA)_2MA_{n-1}Pb_nBr_{3n+1}$ $(n = 1)$		$(BZA)_2MA_{n-1}Pb_nBr_{3n+1}$ $(n = 2)$		$(BZA)_2MA_{n-1}Pb_nBr_{3n+1}$ $(n = 3)$		$(BZA)_2MA_{n-1}Pb_nBr_{3n+1}$ $(n = 4)$		$(BZA)_2MA_{n-1}Pb_nBr_{3n+1}$ $(n = 5)$		$(BZA)_2MA_{n-1}Pb_nBr_{3n+1}$ $(n = 6)$	
Reflection	2θ (°)	d (Å)	2θ (°)	d (Å)	2θ (°)	d (Å)	2θ(°)	d (Å)	2θ (°)	d (Å)	2θ (°)	d (Å)
(002)	5.02	17.60	4.93	17.92	4.3	20.54	4.10	21.55	4.04	21.87	4.04	21.87
(004)	10.3	8.58	9.34	9.46	9.48	9.33	9.24	9.57	9.26	10.32	9.26	10.32

According to Figures 4(b) and 4(e), a slight blue shift in the absorption spectra of 3D-2D $MAPbBr_3$-$A_2MAPbBr_4$ perovskite (A = OA or BZA) is observed in comparison with nonstoichiometric synthesized $MAPbBr_3$ (inset of Figure 4(b)). This suggests the formation of a core-shell type for the mixed 3D-2D perovskites [28]. With increasing n, there is not a significant shift between 3D $MAPbBr_3$ and $A_2MA_{n-1}Pb_nBr_{3n+1}$ perovskite samples for both OA and BZA cations because the fraction of MA in 3D-2D perovskites increases with the rise of n values. Therefore, the optical properties of 3D-2D perovskites tend to be similar to the 3D ones for higher n values. The comparison of absorption spectra between bare and Zn-doped $MAPbBr_3$, shown in the inset of Figure 4(c), points out a blue shift for Zn-doped 3D $MAPbBr_3$ nanostructures. Doping Zn induces unit cell decrement and bandgap increment, resulting in the blue shift [67]. Zn-doped core-shell perovskites (Figures 4(c) and 4(f)) exhibit a similar optical absorption feature to 3D-2D ones (Figures 4(b) and 4(e)). A little blue shift is also observed for 3D-2D Zn-doped $MAPbBr_3 - A_2MA_{n-1}Pb_nBr_{3n+1}$ samples (A = OA, BZA), compared to Zn-doped $MAPbBr_3$, describing the feature of core-shell structure. Consequently, the absorption spectra of all the synthesized 3D-2D perovskites shift to longer wavelengths with respect to 2D ones, due to the presence of 3D perovskites.

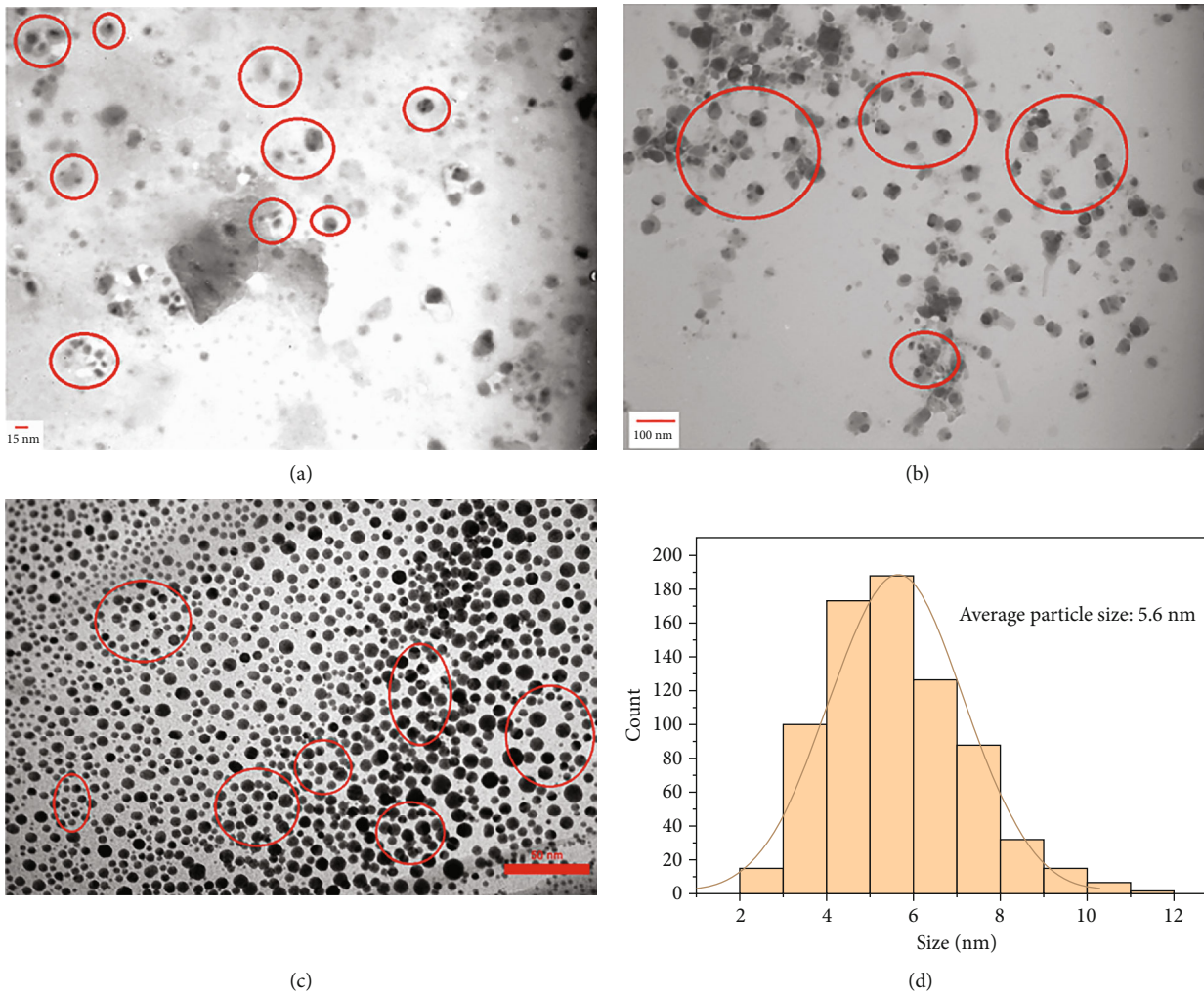

FIGURE 3: TEM images of (a) $MAPbBr_3 - (OA)_2MA_{n-1}Pb_nBr_{3n+1}$ ($n = 6$), (b) Zn-doped $MAPbBr_3 - (BZA)_2MA_{n-1}Pb_nBr_{3n+1}$ ($n = 6$), and (c) $MAPbBr_3 - (BZA)_2MA_{n-1}Pb_nBr_{3n+1}$ ($n = 1$) perovskite NPs and (d) size distribution of $MAPbBr_3 - (BZA)_2MA_{n-1}Pb_nBr_{3n+1}$ ($n = 1$) perovskite.

The PL spectra of synthesized perovskites are depicted in Figure 5. A weak PL peak positioning at 408 nm (inset of Figure 5(a)) corresponds to $(OA)_2PbBr_4$. The PL peak red shifts to 451 nm and 478 nm for OA- and BZA-based 2D $A_2MA_{n-1}Pb_nBr_{3n+1}$ perovskite materials with increasing n values (Figures 5(a) and 5(d)). The maximum PL intensity is related to the sample with $n = 6$.

As shown in Figures 5(b) and 5(e), a red shift in PL peaks of core-shell perovskites with increasing n values originates from the layered nature of 2D perovskites. For the OA- and BZA-based 3D-2D core-shell perovskites, the PL peak starts at 483 nm and 480 nm for $n = 1$ and continues to 494 nm and 491 nm for $n = 6$, respectively. The PL peaks shift to longer wavelengths for 3D-2D nanostructures, with respect to 2D perovskites (Figure 5(a)).

The PL spectra for the nonstoichiometric synthesized $MAPbBr_3$ NPs with an emission peak at 496 nm are given in the inset of Figure 5(b). The blue shift in PL spectra of core-shell $MAPbBr_3 - A_2MA_{n-1}Pb_nBr_{3n+1}$ nanostructures, with respect to 3D $MAPbBr_3$ NPs, relates to the core-shell nature of mixed 3D-2D perovskites [68]. A noticeable enhancement in PL emission spectra is also observed for mixed 3D-2D structures shown in Figure 5(b) due to the presence of $MAPbBr_3$ NPs. Comparing the PL results for OA- and BZA-based perovskites illustrates the PL intensity enhancement for BZA-based perovskites, given in the inset of Figures 5(d)–5(f) for the 2D, mixed 3D-2D, and Zn-doped 3D-2D perovskites, respectively.

Doping Zn into $MAPbBr_3$ perovskite NPs leads to an enhanced and a slight blue-shifted PL peak (at 503 nm) compared to pristine $MAPbBr_3$ NPs (at 507 nm), which is illustrated in the inset of Figure 4(c). The existence of Zn reduces the perovskite defect density and increases the radiative recombination. High-qualified crystallinity and lattice contraction, confirmed by XRD analysis, are responsible for the blue shifting of the PL peak [69, 70]. The blue shift in PL peak position of Zn-doped 3D-2D perovskites with respect to Zn-doped $MAPbBr_3$ NPs refers to the formation of core-shell structures. Zn-doped 3D-2D perovskites show a red shift in PL peaks with increasing n values. Since the highest PL intensity in 2D $A_2MA_{n-1}Pb_nBr_{3n+1}$ perovskites belongs to the $n = 6$ one (Figure 5(a)), mixing them with

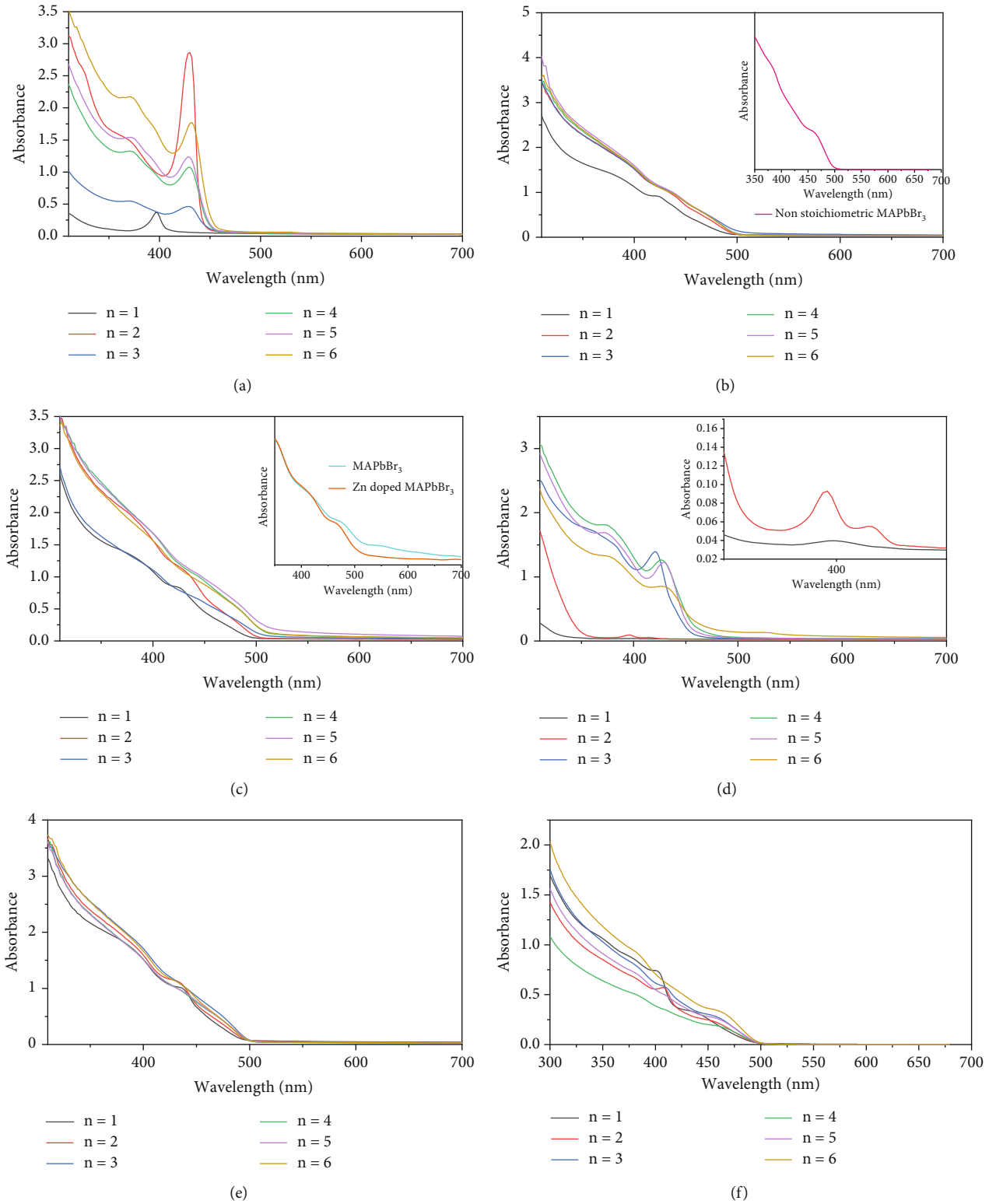

FIGURE 4: Absorption spectra of (a) 2D $(OA)_2MA_{n-1}Pb_nBr_{3n+1}$ ($n = 1 - 6$), (b) 3D-2D core-shell $MAPbBr_3 - (OA)_2MA_{n-1}Pb_nBr_{3n+1}$ ($n = 1 - 6$), (c) Zn-doped 3D-2D core-shell $MAPbBr_3 - (OA)_2MA_{n-1}Pb_nBr_{3n+1}$ ($n = 1 - 6$), (d) 2D $(BZA)_2MA_{n-1}Pb_nBr_{3n+1}$ ($n = 1 - 6$), (e) 3D-2D core-shell $MAPbBr_3 - (BZA)_2MA_{n-1}Pb_nBr_{3n+1}$ ($n = 1 - 6$), and (f) Zn-doped 3D-2D core-shell $MAPbBr_3 - (BZA)_2MA_{n-1}Pb_nBr_{3n+1}$ ($n = 1 - 6$).

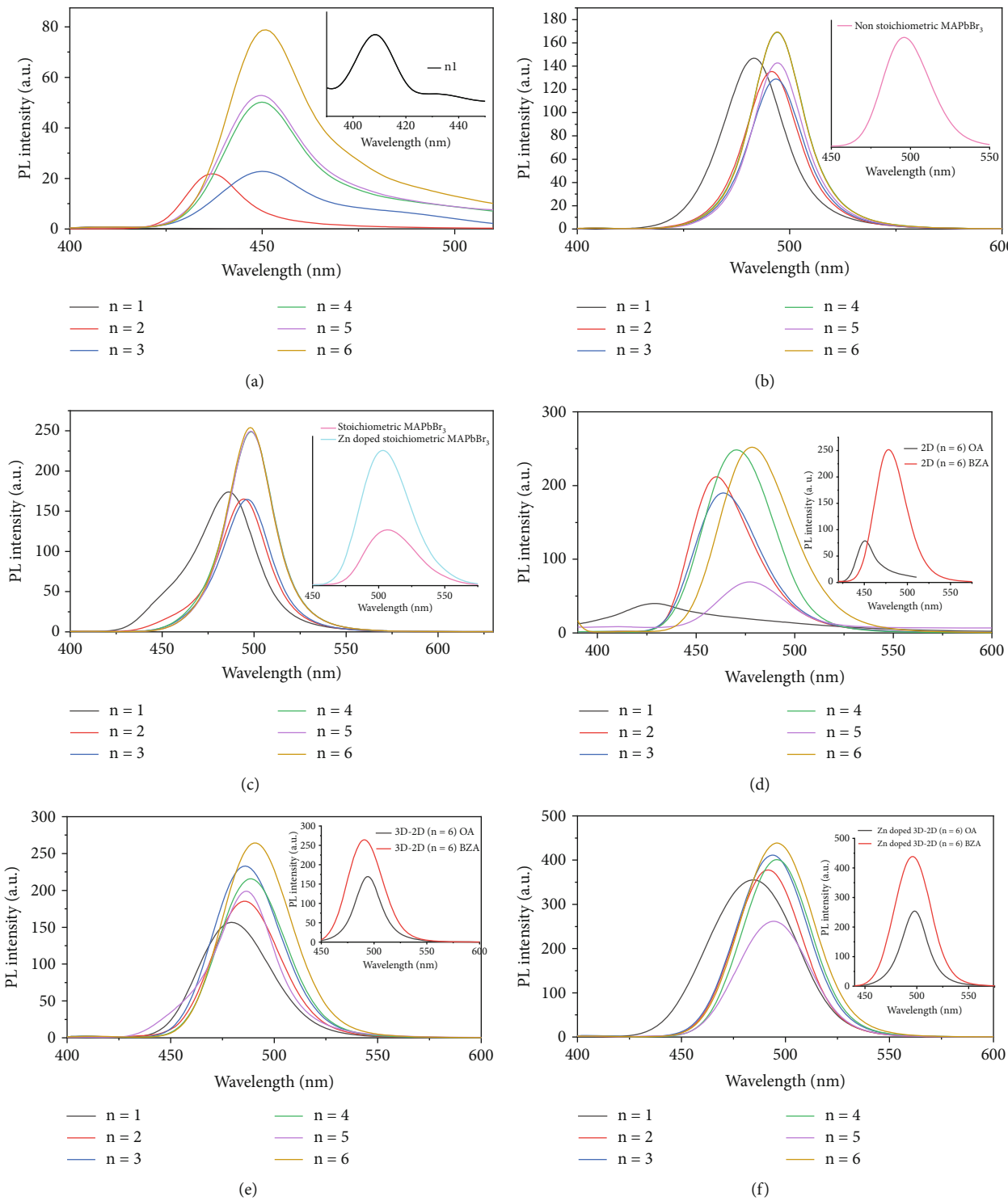

FIGURE 5: PL emission spectra of (a) 2D $(OA)_2MA_{n-1}Pb_nBr_{3n+1}$ $(n = 1 - 6)$, (b) 3D-2D core-shell $MAPbBr_3 - (OA)_2MA_{n-1}Pb_nBr_{3n+1}$ $(n = 1 - 6)$, (c) Zn-doped 3D-2D core-shell $MAPbBr_3 - (OA)_2MA_{n-1}Pb_nBr_{3n+1}$ $(n = 1 - 6)$, (d) 2D $(BZA)_2MA_{n-1}Pb_nBr_{3n+1}$ $(n = 1 - 6)$, (e) 3D-2D core-shell $MAPbBr_3 - (BZA)_2MA_{n-1}Pb_nBr_{3n+1}$ $(n = 1 - 6)$, and (f) Zn-doped 3D-2D core-shell $MAPbBr_3 - (BZA)_2MA_{n-1}Pb_nBr_{3n+1}$ $(n = 1 - 6)$.

3D perovskites gives the highest luminescence to $MAPbBr_3 - A_2MA_{n-1}Pb_nBr_{3n+1}$ with $n = 6$.

Figure 6 represents the light emission of BZA-based nanoperovskites kept in ambient conditions for 20 days. The PL emission of 2D perovskites is reduced significantly, except for the samples with $n = 4$ and $n = 6$ (Figure 6(a)). For core-shell perovskites, the luminescence remains stable after 20 days. Zn-doped core-shell structures show bright

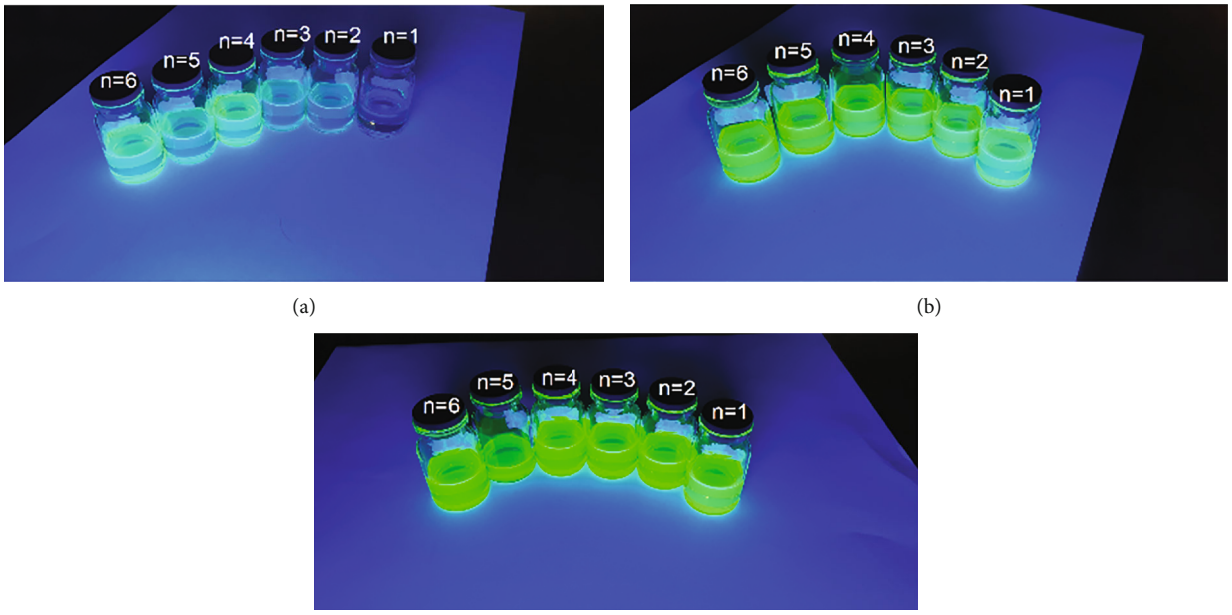

Figure 6: PL emission of (a) $(BZA)_2MA_{n-1}Pb_nBr_{3n+1}$ ($n = 1 - 6$), (b) $MAPbBr_3 - (BZA)_2MA_{n-1}Pb_nBr_{3n+1}$ ($n = 1 - 6$), and (c) Zn-doped $MAPbBr_3 - (BZA)_2MA_{n-1}Pb_nBr_{3n+1}$ ($n = 1 - 6$) perovskites under the illumination of UV lamp after 20 days kept in ambient condition.

Table 3: Calculated PLQY for the synthesized perovskites.

Sample	PLQY
$(OA)_2MA_{n-1}Pb_nBr_{3n+1}$ ($n = 6$)	29%
$MAPbBr_3 - (OA)_2MA_{n-1}Pb_nBr_{3n+1}$ ($n = 6$)	44%
$MAPbBr_3 - (OA)_2MA_{n-1}Pb_nBr_{3n+1}$ ($n = 6$) in the presence of $ZnBr_2$	62%
$(BZA)_2MA_{n-1}Pb_nBr_{3n+1}$ ($n = 6$)	50%
$MAPbBr_3 - (BZA)_2MA_{n-1}Pb_nBr_{3n+1}$ ($n = 6$)	81%
$MAPbBr_3 - (BZA)_2MA_{n-1}Pb_nBr_{3n+1}$ ($n = 6$) in the presence of $ZnBr_2$	94%
$MAPbBr_3$	54%
$MAPbBr_3$ in the presence of $ZnBr_2$	70%

luminescence like the first day of synthesis, as shown in Figure 6(c). The enhanced stability of these perovskites is attributed to the presence of Zn and the core-shell nature of the samples.

3.4. PLQY. The comparative method is used to obtain the PLQY of the synthesized nanoperovskites that are dispersed in toluene [71]. Coumarin 460 is selected as a standard reference dye (PLQY = 73% in ethanol) due to the relative overlap of its emission spectrum with the emission spectra of our synthesized perovskites [72]. For each synthesized perovskite, the absorbance and PL spectra are measured with an excitation wavelength of 373 nm at different concentrations in toluene. The same measurements are conducted for the reference Coumarin 460 in ethanol. The PLQY is obtained by the following equation:

$$\mathrm{PLQY_S} = \mathrm{PLQY_R} \times \frac{I_S}{I_R} \times \frac{A_R}{A_S} \times \frac{n_S^2}{n_R^2}, \quad (1)$$

where I_S and I_R are the integrated areas of PL intensity; A_S and A_R are the absorbance at the excitation wavelength for the perovskite samples (S) and reference (R), respectively; I_S/A_S and I_R/A_R are the slopes of the integrated area of PL intensity versus absorbance, obtained from the measurement of PL, and absorbance spectra at different concentrations, the same for the sample and reference; and n is refractive index, which is 1.497 and 1.362 for toluene and ethanol, respectively. All of the measurements are carried out at room temperature. By calculating the slopes and inserting the values of n (for the sample and reference) and $\mathrm{PLQY_R}$, the PLQY of the sample is obtained.

Calculations of PLQY for the 2D perovskites ($n = 6$), 3D-2D core-shells ($n = 6$), and 3D ones are reported in Table 3. As it is observed in Figure 5, the perovskites containing BZA cation possess greater luminescence intensity than OA-based perovskites, which is verified by PLQY calculations. Substituting BZA cations with OA cations enhances the PLQY by more than 1.5 times. The reason for this can be

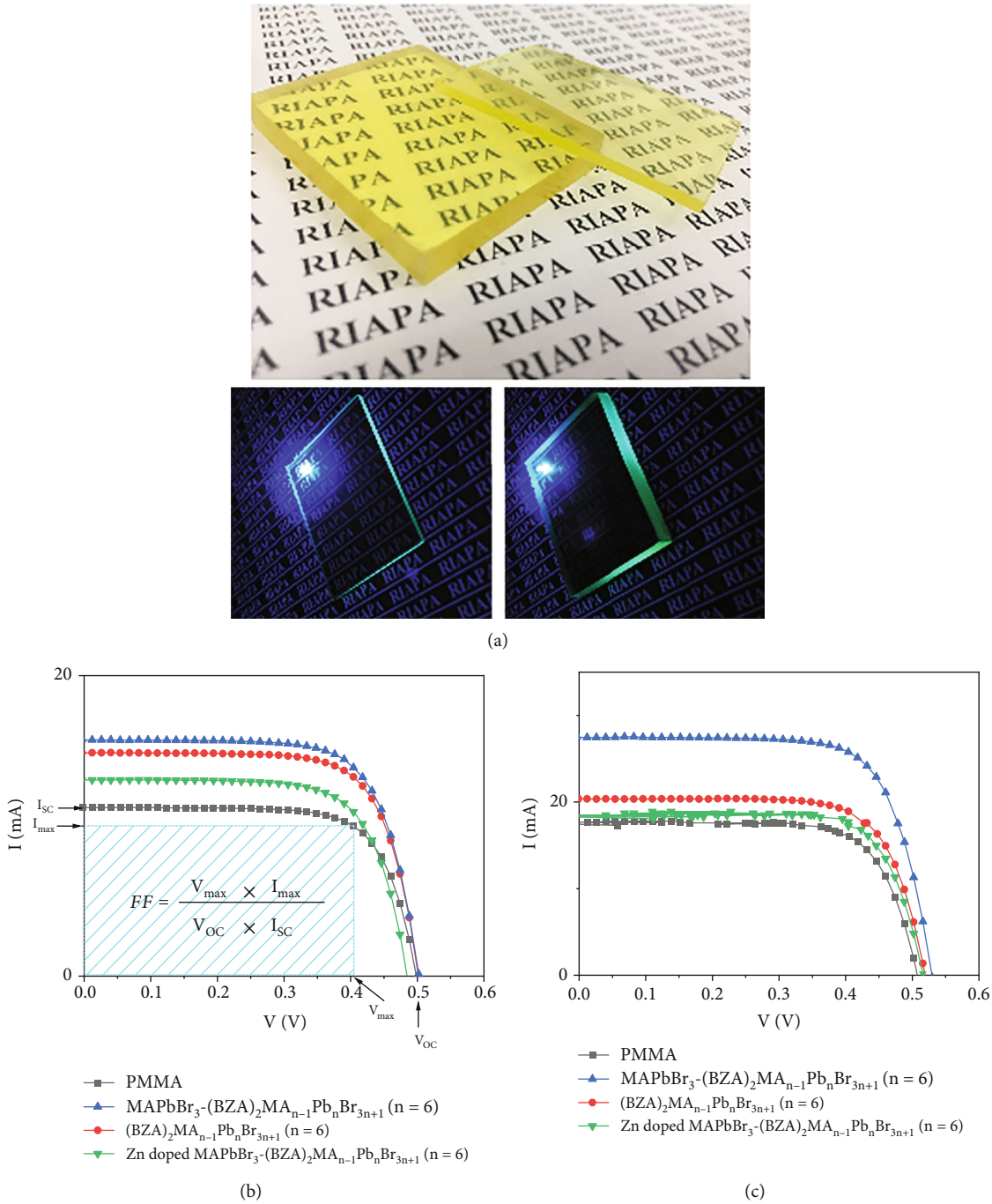

Figure 7: (a) (Top) Fabricated LSCs based on $(BZA)_2MA_{n-1}Pb_nBr_{3n+1}$ ($n = 6$) with thicknesses of 2 mm and 5 mm and (bottom) their emission under incident laser light, I-V curves of the solar panel attached to the LSCs based on PMMA, $(BZA)_2MA_{n-1}Pb_nBr_{3n+1}$ ($n = 6$), $MAPbBr_3 - (BZA)_2MA_{n-1}Pb_nBr_{3n+1}$ ($n = 6$), and Zn-doped $MAPbBr_3 - (BZA)_2MA_{n-1}Pb_nBr_{3n+1}$ ($n = 6$) core-shell with thicknesses of (b) 2 mm and (c) 5 mm.

attributed to the special chemical structure of benzene, which causes surface passivation of surface defects by reducing trap states. Therefore, the radiative recombination rate is increased [73, 74]. Also, the samples containing 3D-2D multidimensional perovskite NPs have a higher emission intensity than 2D samples, which is true for both categories where OA or BZA cations are used. The PLQY for core-shell 3D-2D perovskites containing OA and BZA is increased by over 1.5-fold and nearly twofold versus their 2D counterparts, respectively. It is clear that $ZnBr_2$ also has a significant effect on improving the PLQY of the synthesized nanoperovskites. For comparison, the PLQY for 3D perovskites is also given in Table 3. The maximum PLQY is obtained for the Zn-doped 3D-2D perovskites with $n = 6$.

3.5. LSC Characterization. In order to show the performance of our synthesized highly luminescent perovskites in optoelectronic applications, they are utilized in LSCs. Due to

Table 4: The PV panel parameters attached to the LSCs with thickness of 2 mm.

LSC	V_{OC} (mV)	I_{SC} (mA)	FF (%)	PCE (%)	ΔPCE (%)
PMMA	0.498	11.22	72.1	0.97	—
$(BZA)_2MA_{n-1}Pb_nBr_{3n+1}$ $(n=6)$	0.501	14.86	71.9	1.29	32.9
$MAPbBr_3 - (BZA)_2MA_{n-1}Pb_nBr_{3n+1}$ $(n=6)$	0.502	15.72	71.3	1.36	40.2
Zn – doped $MAPbBr_3 - (BZA)_2MA_{n-1}Pb_nBr_{3n+1}$ $(n=6)$	0.484	13.05	71	1.08	11.3

Table 5: The PV panel parameters attached to the LSCs with thickness of 5 mm.

LSC	V_{OC} (mV)	I_{SC} (mA)	FF (%)	PCE (%)	ΔPCE (%)
PMMA	0.51	17.3	74.4	1.59	—
$(BZA)_2MA_{n-1}Pb_nBr_{3n+1}$ $(n=6)$	0.519	20.36	72.3	1.85	16.3
$MAPbBr_3 - (BZA)_2MA_{n-1}Pb_nBr_{3n+1}$ $(n=6)$	0.529	27.46	72.2	2.54	59.7
Zn – doped $MAPbBr_3 - (BZA)_2MA_{n-1}Pb_nBr_{3n+1}$ $(n=6)$	0.522	18.01	76.3	1.74	9.4

the higher luminescence emission of BZA nanoperovskites versus OA ones, BZA perovskites are utilized as luminescent fluorophores in the manufactured LSCs. Optical properties studies show a wider absorption spectral range and higher PL emission for $n=6$ of each category between different n values. Therefore, for 2D and 3D-2D perovskites, the sample with $n=6$ is embedded into LSCs.

The fabricated LSCs with dimensions of $50\times40\times5\,mm^3$ and $50\times40\times2\,mm^3$ doped with 2D $(BZA)_2MA_{n-1}Pb_nBr_{3n+1}$ $(n=6)$ and core-shell $MAPbBr_3 - (BZA)_2MA_{n-1}Pb_nBr_{3n+1}$ $(n=6)$ nanoperovskites are characterized by attaching a PV panel to one of the LSC edges. As an example, Figure 7(a) demonstrates 2D $(BZA)_2MA_{n-1}Pb_nBr_{3n+1}$ $(n=6)$-based LSCs with thicknesses of 2 mm and 5 mm, in which the luminescence of the LSCs from the edges is noticeable under illumination of a diode laser with a 437 nm wavelength. To characterize the LSCs with 2 mm thickness, the excessive area of the PV panel is marked with a black tape. Therefore, the remaining area of the PV panel to be attached to the 2 mm LSC is $3.8\times0.2\,cm^2$. The PV parameters of the fabricated LSC devices are presented in Figure 7 and Tables 4 and 5.

Comparison of I-V curves for 2D and core-shell 3D-2D-based LSC devices reveals higher I_{SC} for $MAPbBr_3 - (BZA)_2MA_{n-1}Pb_nBr_{3n+1}$ $(n=6)$-based LSCs than 2D LSCs (Figures 7(b) and 7(c)). This trend is identical for both LSC thicknesses. Higher PLQY of core-shell structure versus 2D nanoperovskites improves the amount of emission light reached to the LSC edges, hence enhance I_{SC} [75]. For thick LSCs, the solar harvesting capability is boosted [76]. Consequently, the power conversion efficiency (PCE) for 5 mm LSC devices is higher than the PCE of thin devices. Characteristics of PV panel in adjacent to blank PMMA LSCs are also presented in Tables 4 and 5. It is obvious that the LSCs based on $MAPbBr_3 - (BZA)_2MA_{n-1}Pb_nBr_{3n+1}$ $(n=6)$ perovskites perform better than other LSCs.

Although the LSCs based on Zn-doped 3D-2D perovskites possess the highest PLQY among the synthesized perovskites in this paper, the PCE values for these devices are low. This result is realized for all the Zn-doped perovskite LSCs. To understand, Zn-doped perovskites and their mixture with PMMA are prepared, and their optical properties are studied. No change in PL emission is observed for any of the solutions, which implies that PMMA has no side effect on perovskite PL emission. It seems that the polymerization process is responsible for the low performance of Zn-doped perovskite LSCs. When $ZnBr_2$ is incorporated into a polymer solution, some chemical reactions occur during the polymerization process and destabilize the polymer [77]. It seems that this process results in reduced PL emission of Zn-doped perovskites.

4. Conclusion

2D perovskites with octylamine and benzylamine cations are successfully synthesized, and the highest PL emission belongs to the samples with $n=6$. Core-shell nanoperovskites are also prepared by mixing 3D and 2D perovskites. The average size of $MAPbBr_3$-$(BZA)_2PbBr_4$ perovskite is obtained 5.6 nm from the TEM image. Benzylamine-based perovskites exhibit higher PLQY than octylamine-based ones. In addition to enhanced emission intensity, a positive impact of doping Zn is an improved stability. The highest PLQY (94%) is recorded for the Zn-doped $MAPbBr_3 - (BZA)_2MA_{n-1}Pb_nBr_{3n+1}$ $(n=6)$ perovskite. Doping highly luminescent perovskites into LSC devices enhances their performance. The LSCs are fabricated in 2 mm and 5 mm thicknesses. Thick LSCs show higher PCE than thin ones, due to the improvement of the solar harvesting capability in 5 mm LSCs. Among 2 mm LSCs, the best result is obtained for the LSC containing mixed 3D-2D perovskite with a relative PCE value of 40.2%. The performance of the mixed 3D-2D perovskite-based LSC with 5 mm thickness is the greatest, with a relative PCE yield of up to 60%. Although the Zn-doped perovskites have the highest PLQY with respect to the undoped samples, their fabricated LSCs demonstrate lower PCE values. This is due to the polymerization process, which occurs in Zn-doped perovskites and results in destabilizing the LSC.

Data Availability

Data will be made available on request.

Conflicts of Interest

The authors declare that they have no conflicts of interest.

References

[1] W. Deng, H. Fang, X. Jin, X. Zhang, X. Zhang, and J. Jie, "Organic-inorganic hybrid perovskite quantum dots for light-emitting diodes," *Journal of Materials Chemistry C*, vol. 6, no. 18, pp. 4831–4841, 2018.

[2] P. Lu, M. Lu, H. Wang et al., "Metal halide perovskite nanocrystals and their applications in optoelectronic devices," *InfoMat*, vol. 1, no. 4, pp. 430–459, 2019.

[3] H. Zhao, Y. Zhou, D. Benetti, D. Ma, and F. Rosei, "Perovskite quantum dots integrated in large-area luminescent solar concentrators," *Nano Energy*, vol. 37, pp. 214–223, 2017.

[4] Z. Liu, B. Zhang, and Y. Chen, "Recent progress in two-dimensional nanomaterials for laser protection," *Chemistry*, vol. 1, no. 1, pp. 17–43, 2019.

[5] M. V. Kovalenko, L. Protesescu, and M. I. Bodnarchuk, "Properties and potential optoelectronic applications of lead halide perovskite nanocrystals," *Science*, vol. 358, no. 6364, pp. 745–750, 2017.

[6] J. Pan, F. Fang, J. Xie et al., "Synergistic effects of charge transport engineering and passivation enabling efficient inverted perovskite quantum-dot light-emitting diodes," *Journal of Materials Chemistry C*, vol. 8, no. 16, pp. 5572–5579, 2020.

[7] A. Mehta, J. Im, B. H. Kim, H. Min, R. Nie, and S. Il Seok, "Stabilization of lead-tin-alloyed inorganic-organic halide perovskite quantum dots," *ACS Nano*, vol. 12, no. 12, pp. 12129–12139, 2018.

[8] Y. Fu, H. Zhu, A. W. Schrader et al., "Nanowire lasers of formamidinium lead halide perovskites and their stabilized alloys with improved stability," *Nano Letters*, vol. 16, no. 2, pp. 1000–1008, 2016.

[9] Y. Han, S. Yue, and B.-B. Cui, "Low-dimensional metal halide perovskite crystal materials: structure strategies and luminescence applications," *Advanced Science*, vol. 8, no. 15, pp. 1–21, 2021.

[10] G. Grancini and M. K. Nazeeruddin, "Dimensional tailoring of hybrid perovskites for photovoltaics," *Nature Reviews Materials*, vol. 4, no. 1, pp. 4–22, 2019.

[11] P. Gao, A. R. B. M. Yusoff, and M. K. Nazeeruddin, "Dimensionality engineering of hybrid halide perovskite light absorbers," *Nature Communications*, vol. 9, no. 1, p. 5028, 2018.

[12] T. Liu, Z. Zhang, Q. Wei et al., "Tailoring quasi-2D perovskite thin films via nanocrystals mediation for enhanced electroluminescence," *Chemical Engineering Journal*, vol. 411, article 128511, 2021.

[13] D. Xu, Q. Wan, S. Wu et al., "Enhancing the performance of LARP-synthesized CsPbBr3nanocrystal LEDs by employing a dual hole injection layer," *RSC Advances*, vol. 10, no. 30, pp. 17653–17659, 2020.

[14] F. Zhang, H. Zhong, C. Chen et al., "Brightly luminescent and color-tunable colloidal CH3NH3PbX3 (X = Br, I, Cl) quantum dots: potential alternatives for display technology," *ACS Nano*, vol. 9, no. 4, pp. 4533–4542, 2015.

[15] L. Peng, A. Tang, C. Yang, and F. Teng, "Size-controlled synthesis of highly luminescent organometal halide perovskite quantum dots," *Journal of Alloys and Compounds*, vol. 687, pp. 506–513, 2016.

[16] Y. Yuan, Z. Liu, Z. Liu, L. Peng, Y. Li, and A. Tang, "Photoluminescence and self-assembly of cesium lead halide perovskite nanocrystals: effects of chain length of organic amines and reaction temperature," *Applied Surface Science*, vol. 405, pp. 280–288, 2017.

[17] C. H. Lu, J. Hu, W. Y. Shih, and W. H. Shih, "Control of morphology, photoluminescence, and stability of colloidal methylammonium lead bromide nanocrystals by oleylamine capping molecules," *Journal of Colloid and Interface Science*, vol. 484, pp. 17–23, 2016.

[18] J. Dong, Z. Q. Ma, Y. Yang, S. P. Wang, and H. Pan, "Mixed two-dimensional organic-inorganic halide perovskites for highly efficient and stable photovoltaic application," *Molecules*, vol. 24, no. 11, p. 2144, 2019.

[19] Y. Chen, Y. Sun, J. Peng, J. Tang, K. Zheng, and Z. Liang, "2D Ruddlesden–popper perovskites for optoelectronics," *Advanced Materials*, vol. 30, no. 2, pp. 1–15, 2018.

[20] K.-z. Du, Q. Tu, X. Zhang et al., "Two-dimensional lead(II) halide-based hybrid perovskites templated by acene alkylamines: crystal structures, optical properties, and piezoelectricity," *Inorganic Chemistry*, vol. 56, no. 15, pp. 9291–9302, 2017.

[21] Y. H. Chang, J. C. Lin, Y. C. Chen, T. R. Kuo, and D. Y. Wang, "Facile synthesis of two-dimensional Ruddlesden–Popper perovskite quantum dots with fine-tunable optical properties," *Nanoscale Research Letters*, vol. 13, no. 1, p. 247, 2018.

[22] R. Xie, U. Kolb, J. Li, T. Basché, and A. Mews, "Synthesis and characterization of highly luminescent CdSe–Core CdS/Zn0.5Cd0.5S/ZnS multishell nanocrystals," *Journal of the American Chemical Society*, vol. 127, no. 20, pp. 7480–7488, 2005.

[23] Y. Shirasaki, G. J. Supran, M. G. Bawendi, and V. Bulović, "Emergence of colloidal quantum-dot light-emitting technologies," *Nature Photonics*, vol. 7, no. 1, pp. 13–23, 2013.

[24] S. D. Adhikari, A. F. Gualdrón Reyes, S. Paul et al., "Impact of core-shell perovskite nanocrystals for LED applications: successes, challenges, and prospects," *Chemical Science*, vol. 14, no. 34, pp. 8984–8999, 2023.

[25] D. Banerjee and A. Kumar Kar, "Role of acceptor concentration-dependent FRET behind luminescence tuning in polymer capped ZnO for application in hybrid LEDs," *Materials Letters*, vol. 303, 2021.

[26] D. Banerjee and A. Kumar Kar, "Structural strategy to enhance the quantum and photocatalytic efficiency of ZnO quantum dots by incorporation of interface states," *Journal of Photochemistry and Photobiology A: Chemistry*, vol. 437, 2023.

[27] D. Banerjee, P. Banerjee, and A. K. Kar, "Insights into the impact of photophysical processes and defect state evolution on the emission properties of surface-modified ZnO nanoplates for application in photocatalysis and hybrid LEDs," *Physical Chemistry Chemical Physics*, vol. 24, no. 4, pp. 2424–2440, 2022.

[28] S. Bhaumik, S. A. Veldhuis, Y. F. Ng et al., "Highly stable, luminescent core–shell type methylammonium–octylammonium lead bromide layered perovskite nanoparticles," *Chemical Communications*, vol. 52, no. 44, pp. 7118–7121, 2016.

[29] W. Chen, S. Bhaumik, S. A. Veldhuis et al., "Giant five-photon absorption from multidimensional core-shell halide perovskite

colloidal nanocrystals," *Nature Communications*, vol. 8, no. 1, 2017.

[30] C. V. Mary Vijila, K. Rajeev Kumar, and M. K. Jayaraj, "Stokes shift engineered, stable core-shell perovskite nanoparticle - Poly(methyl methacrylate) composites with high photoluminescence quantum yield," *Optical Materials*, vol. 94, pp. 241–248, 2019.

[31] C. Jia, H. Li, X. Meng, and H. Li, "CsPbX3/Cs4PbX6core/shell perovskite nanocrystals," *Chemical Communications*, vol. 54, no. 49, pp. 6300–6303, 2018.

[32] B. Qiao, P. Song, J. Cao et al., "Water-resistant, monodispersed and stably luminescent CsPbBr3/CsPb2Br5core–shell-like structure lead halide perovskite nanocrystals," *Nanotechnology*, vol. 28, no. 44, article 445602, 2017.

[33] D. Banerjee and B. Saparov, "Ultrabright light emission properties of all-inorganic and hybrid organic-inorganic copper(I) halides†," *Chemistry of Materials*, vol. 35, no. 9, pp. 3364–3385, 2023.

[34] L. Lian, X. Wang, P. Zhang et al., "Highly luminescent zero-dimensional organic copper halides for X-ray scintillation," *Journal of Physical Chemistry Letters*, vol. 12, no. 29, pp. 6919–6926, 2021.

[35] D. A. Popy, B. N. Evans, J. Jiang et al., "Intermolecular arrangement facilitated broadband blue emission in group-12 metal (Zn, Cd) hybrid halides and their applications," *Materials Today Chemistry*, vol. 30, p. 101502, 2023.

[36] D. Banerjee, D. A. Popy, B. C. Leininger et al., "Zero-dimensional broadband yellow light emitter (TMS)3Cu2I5for latent fingerprint detection and solid-state lighting," *ACS Applied Materials & Interfaces*, vol. 15, no. 25, pp. 30455–30468, 2023.

[37] D. Banerjee, P. Banerjee, and A. K. Kar, "Structure-correlated excitation wavelength-dependent optical properties of ZnO nanostructures for multifunctional applications," *New Journal of Chemistry*, vol. 47, no. 3, pp. 1142–1155, 2023.

[38] D. Banerjee and A. K. Kar, "Effect of hydroxide ion concentration on the evolution of nanostructures and structure correlated luminescence of ZnO nanopowders," *Optical Materials*, vol. 89, pp. 430–440, 2019.

[39] R. Priya, S. Bhatia, S. Kaur, V. Dubey, and O. P. Pandey, *Defects in rare-earth-doped inorganic materials*, Elsevier Inc., 2022.

[40] Y. J. Guo, J. Su, L. Wang, Z. Lin, Y. Hao, and J. Chang, "Improved doping and optoelectronic properties of Zn-doped Cspbbr3perovskite through Mn codoping approach," *Journal of Physical Chemistry Letters*, vol. 12, no. 13, pp. 3393–3400, 2021.

[41] R. Mayengbam, S. K. Tripathy, and G. Palai, "Structural, electronic, optical and mechanical properties of Zn-doped $MAPbI_3$ perovskites and absorber layer efficiencies: An *ab-initio* investigation," *Materials Today Communications*, vol. 24, article 101216, 2020.

[42] Y. Liu, A. Wang, J. Wu et al., "Alkylamine screening and zinc doping of highly luminescent 2D tin-halide perovskites for LED lighting," *Materials Advances*, vol. 2, no. 4, pp. 1320–1327, 2021.

[43] W. Zhao, D. Yang, Z. Yang, and S. (. F.). Liu, "Zn-doping for reduced hysteresis and improved performance of methylammonium lead iodide perovskite hybrid solar cells," *Materials Today Energy*, vol. 5, pp. 205–213, 2017.

[44] S. Bai, Z. Yuan, and F. Gao, "Colloidal metal halide perovskite nanocrystals: synthesis, characterization, and applications," *Journal of Materials Chemistry C*, vol. 4, no. 18, pp. 3898–3904, 2016.

[45] D. Priante, I. Dursun, M. S. Alias et al., "The recombination mechanisms leading to amplified spontaneous emission at the true-green wavelength in CH3NH3PbBr3 perovskites," *Applied Physics Letters*, vol. 106, no. 8, 2015.

[46] E. V. Ushakova, S. A. Cherevkov, V. A. Kuznetsova, and A. V. Baranov, "Lead-free perovskites for lighting and lasing applications: a minireview," *Materials*, vol. 12, no. 23, p. 3845, 2019.

[47] J. Gutmann, J. Posdziech, M. Peters et al., "Emission of rhodamine B in PMMA opals for luminescent solar concentrators," *Photonics for Solar Energy Systems IV*, vol. 8438, 2012, pp. 84381O–84381O–7, Brussels, Belgium, October 2015.

[48] E. Bagherzadeh-Khajehmarjan, A. Nikniazi, B. Olyaeefar, S. Ahmadi-Kandjani, and J.-M. Nunzi, "Bulk luminescent solar concentrators based on organic-inorganic $CH_3NH_3PbBr_3$ perovskite fluorophores," *Solar Energy Materials & Solar Cells*, vol. 192, pp. 44–51, 2019.

[49] E. Bagherzadeh-Khajehmarjan, S. Mahdieh, and A. Nikniazi, "Boosting the efficiency of luminescent solar concentrator devices based on $CH_3NH_3PbBr_3$ perovskite quantum dots via geometrical parameter engineering and plasmonic coupling," *Organic Electronics*, vol. 109, article 106629, 2022.

[50] J. Wu, J. Tong, Y. Gao et al., "Efficient and stable thin-film luminescent solar concentrators enabled by near-infrared emission perovskite nanocrystals," *Angewandte Chemie International Edition*, vol. 59, no. 20, pp. 7738–7742, 2020.

[51] Y. Liu, N. Li, R. Sun et al., "Stable metal-halide perovskites for luminescent solar concentrators of real- device integration," *Nano Energy*, vol. 85, article 105960, 2021.

[52] Z. Li, A. Johnston, M. Wei et al., "Solvent-solute coordination engineering for efficient perovskite luminescent solar concentrators," *Joule*, vol. 4, no. 3, pp. 631–643, 2020.

[53] V. Charlot, A. Ibrahim, X. Allonas, C. Croutxé-Barghorn, and C. Delaite, "Photopolymerization of methyl methacrylate: effects of photochemical and photonic parameters on the chain length," *Polymer Chemistry*, vol. 5, no. 21, pp. 6236–6243, 2014.

[54] M. G. Debije, R. C. Evans, and G. Griffini, "Laboratory protocols for measuring and reporting the performance of luminescent solar concentrators," *Energy & Environmental Science*, vol. 14, no. 1, pp. 293–301, 2021.

[55] Y. Tabuchi, K. Asai, M. Rikukawa, K. Sanui, and K. Ishigure, "Preparation and characterization of natural lower dimensional layered perovskite-type compounds," *Journal of Physics and Chemistry of Solids*, vol. 61, no. 6, pp. 837–845, 2000.

[56] M. Li, Q. Wei, S. K. Muduli et al., "Enhanced exciton and photon confinement in Ruddlesden-Popper perovskite microplatelets for highly stable low-threshold polarized lasing," *Advanced Materials*, vol. 30, no. 23, article 1707235, 2018.

[57] S. Aharon and L. Etgar, "Two dimensional organometal halide perovskite nanorods with tunable optical properties," *Nano Letters*, vol. 16, no. 5, pp. 3230–3235, 2016.

[58] C. C. Stoumpos, D. H. Cao, D. J. Clark et al., "Ruddlesden-popper hybrid Lead iodide perovskite 2D homologous semiconductors," *Chemistry of Materials*, vol. 28, no. 8, pp. 2852–2867, 2016.

[59] Z. Yuan, Y. Shu, Y. Xin, and B. Ma, "Highly luminescent nanoscale quasi-2D layered lead bromide perovskites with tunable emissions," *Chemical Communications*, vol. 52, no. 20, pp. 3887–3890, 2016.

[60] X. Yang, X. Zhang, J. Deng et al., "Efficient green light-emitting diodes based on quasi-two-dimensional composition and phase engineered perovskite with surface passivation," *Nature Communications*, vol. 9, no. 1, pp. 570–579, 2018.

[61] N. Yantara, A. Bruno, A. Iqbal et al., "Designing efficient energy funneling kinetics in Ruddlesden–Popper Perovskites for high-performance light-emitting diodes," *Advanced Materials*, vol. 30, no. 33, article 1800818, 2018.

[62] Z. Yan, J. S. Benas, C. C. Chueh et al., "Stable blue perovskite light-emitting diodes achieved by optimization of crystal dimension through zinc bromide addition," *Chemical Engineering Journal*, vol. 414, article 128774, 2021.

[63] Z. Yuan, Y. Shu, Y. Tian, Y. Xin, and B. Ma, "A facile one-pot synthesis of deep blue luminescent lead bromide perovskite microdisks," *Chemical Communications*, vol. 51, no. 91, pp. 16385–16388, 2015.

[64] B.-E. Cohen, M. Wierzbowska, and L. Etgar, "High efficiency quasi 2D lead bromide perovskite solar cells using various barrier molecules," *Sustainable Energy & Fuels*, vol. 1, no. 9, pp. 1935–1943, 2017.

[65] S. Gonzalez-Carrero, G. M. Espallargas, R. E. Galian, and J. Pérez-Prieto, "Blue-luminescent organic lead bromide perovskites: highly dispersible and photostable materials," *Journal of Materials Chemistry A*, vol. 3, no. 26, pp. 14039–14045, 2015.

[66] N. Wang, L. Cheng, R. Ge et al., "Perovskite light-emitting diodes based on solution-processed self-organized multiple quantum wells," *Nature Photonics*, vol. 10, no. 11, pp. 699–704, 2016.

[67] R. Li, S. Chen, X. Li et al., "Zn doped MAPbBr3single crystal with advanced structural and optical stability achieved by strain compensation," *Nanoscale*, vol. 12, no. 6, pp. 3692–3700, 2020.

[68] S. Ray, A. Mohapatra, and S. Bhaumik, "Synthesis of highly stable double-coated Zn-doped cesium lead bromide nanocrystals for indium ion detection in water," *Materials Advances*, vol. 3, no. 11, pp. 4684–4692, 2022.

[69] S. Parveen and P. K. Giri, "Emerging doping strategies in two-dimensional hybrid perovskite semiconductors for cutting edge optoelectronics applications," *Nanoscale Advances*, vol. 4, no. 4, pp. 995–1025, 2022.

[70] V. Naresh and N. Lee, "Zn(II)-doped cesium lead halide perovskite nanocrystals with high quantum yield and wide color tunability for color-conversion light-emitting displays," *ACS Applied Nano Materials*, vol. 3, no. 8, pp. 7621–7632, 2020.

[71] J. Laverdant, W. D. . Marcillac, C. Barthou et al., "Experimental determination of the fluorescence quantum yield of semiconductor nanocrystals," *Materials*, vol. 4, no. 7, pp. 1182–1193, 2011.

[72] G. Jones, W. R. Jackson, C. Y. Choi, and W. R. Bergmark, "Solvent effects on emission yield and lifetime for Coumarin laser dyes. Requirements for a rotatory decay mechanism," *The Journal of Physical Chemistry*, vol. 89, no. 2, pp. 294–300, 1985.

[73] G. Liu, X. X. Xu, S. Xu et al., "Passivation effect of halogenated benzylammonium as a second spacer cation for improved photovoltaic performance of quasi-2D perovskite solar cells," *Journal of Materials Chemistry A*, vol. 8, no. 12, pp. 5900–5906, 2020.

[74] H. Lu, A. Krishna, S. M. Zakeeruddin, M. Grätzel, and A. Hagfeldt, "Compositional and interface engineering of organic-inorganic lead halide perovskite solar cells," *IScience*, vol. 23, no. 8, pp. 1–14, 2020.

[75] H. Zhao, D. Benetti, L. Jin, Y. Zhou, F. Rosei, and A. Vomiero, "Absorption enhancement in 'giant' core/alloyed-shell quantum dots for luminescent solar concentrator," *Small*, vol. 12, no. 38, pp. 5354–5365, 2016.

[76] F. Meinardi, S. Ehrenberg, L. Dhamo et al., "Highly efficient luminescent solar concentrators based on earth-abundant indirect-bandgap silicon quantum dots," *Nature Photonics*, vol. 11, no. 3, pp. 177–185, 2017.

[77] I. C. McNeill and R. C. McGuiness, "The effect of zinc bromide on the thermal degradation of poly(methyl methacrylate): part 2–reaction products, structural changes and degradation mechanism," *Polymer Degradation and Stability*, vol. 9, no. 4, pp. 209–224, 1984.